Cascadable excitability in microrings

Thomas Van Vaerenbergh,[1,3,*] **Martin Fiers,**[1,3] **Pauline Mechet,**[1,3] **Thijs Spuesens,**[1,3] **Rajesh Kumar,**[1,3] **Geert Morthier,**[1,3] **Benjamin Schrauwen,**[2] **Joni Dambre,**[2] **and Peter Bienstman**[1,3]

[1]*Photonics Research Group (INTEC), Ghent University - imec,*
Sint-Pietersnieuwstraat 41, B-9000 Ghent, Belgium
[2]*Electronics and Information Systems (ELIS), Ghent University,*
Sint-Pietersnieuwstraat 41, B-9000 Ghent, Belgium
[3]*Center for Nano- and Biophotonics (NB-Photonics), Ghent University,*
Sint-Pietersnieuwstraat 41, B-9000 Ghent, Belgium
*[*thomas.vanvaerenbergh@intec.ugent.be](mailto:thomas.vanvaerenbergh@intec.ugent.be)*

Abstract: To emulate a spiking neuron, a photonic component needs to be excitable. In this paper, we theoretically simulate and experimentally demonstrate cascadable excitability near a self-pulsation regime in high-Q-factor silicon-on-insulator microrings. For the theoretical study we use Coupled Mode Theory. While neglecting the fast energy and phase dynamics of the cavity light, we can still preserve the most important microring dynamics, by only keeping the temperature difference with the surroundings and the amount of free carriers as dynamical variables of the system. Therefore we can analyse the microring dynamics in a 2D phase portrait. For some wavelengths, when changing the input power, the microring undergoes a subcritical Andronov-Hopf bifurcation at the self-pulsation onset. As a consequence the system shows class II excitability. Experimental single ring excitability and self-pulsation behaviour follows the theoretic predictions. Moreover, simulations and experiments show that this excitation mechanism is cascadable.

OCIS codes: (190.1450) Bistability; (190.4390) Nonlinear optics, integrated optics; (190.4870) Optically induced thermo-optical effects; (200.4700) Optical neural systems; (230.1150) All-optical devices; (230.4555) Coupled resonators.

References and links

1. K. Vandoorne, J. Dambre, D. Verstraeten, B. Schrauwen, and P. Bienstman, "Parallel reservoir computing using optical amplifiers," IEEE Trans. Neural Netw. **22**, 1469–1481 (2011).
2. W. Maass, T. Natschläger, and H. Markram, "Real-time computing without stable states: A new framework for neural computation based on perturbations," Neural Comput. **14**, 2531–2560 (2002).
3. E. M. Izhikevich, *Dynamical Systems in Neuroscience: The Geometry of Excitability and Bursting (Computational Neuroscience)*, 1st ed. (The MIT Press, 2006).
4. M. Brunstein, A. Yacomotti, I. Sagnes, F. Raineri, L. Bigot, and A. Levenson, "Excitability and self-pulsing in a photonic crystal nanocavity," Phys. Rev. A **85**, 1–5 (2012).
5. W. Coomans, L. Gelens, S. Beri, J. Danckaert, and G. Van der Sande, "Solitary and coupled semiconductor ring lasers as optical spiking neurons," Phys. Rev. E **84**, 1–8 (2011).
6. G. Priem, P. Dumon, W. Bogaerts, D. Van Thourhout, G. Morthier, and R. Baets, "Optical bistability and pulsating behaviour in Silicon-On-Insulator ring resonator structures," Opt. Express **13**, 9623–9628 (2005).
7. A. Yacomotti, P. Monnier, F. Raineri, B. Bakir, C. Seassal, R. Raj, and J. Levenson, "Fast Thermo-Optical Excitability in a Two-Dimensional Photonic Crystal," Phys. Rev. Lett. **97**, 6–9 (2006).
8. W. H. P. Pernice, M. Li, and H. X. Tang, "Time-domain measurement of optical transport in silicon micro-ring resonators," Opt. Express **18**, 18438–18452 (2010).

9. T. J. Johnson, M. Borselli, and O. Painter, "Self-induced optical modulation of the transmission through a high-Q silicon microdisk resonator," Opt. Express **14**, 817–831 (2006).
10. Q. Lin, T, J. Johnson, C. P. Michael, and O. Painter, "Adiabatic self-tuning in a silicon microdisk optical resonator," Opt. Express **16**, 14801–14811 (2008).
11. M. Fiers, T. Van Vaerenbergh, K. Caluwaerts, D. Vande Ginste, B. Schrauwen, J. Dambre, and P. Bienstman, "Time-domain and frequency-domain modeling of nonlinear optical components on circuit-level using a node-based approach," J. Opt. Soc. Am. B **29**, 896–900 (2011).
12. P. Barclay, K. Srinivasan, and O. Painter, "Nonlinear response of silicon photonic crystal microresonators excited via an integrated waveguide and fiber taper," Opt. Express **13**, 801–820 (2005).
13. J. Guckenheimer, and P. Holmes, *Nonlinear Oscillations, Dynamical Systems and Bifurcation of Vector Fields*, 2nd ed. (Springer-Verlag, 1983).
14. R. H. Clewley, W. E. Sherwood, M. D. LaMar, and J. M. Guckenheimer "PyDSTool, a software environment for dynamical systems modeling," http://pydstool.sourceforge.net, (2007).
15. A. F. Oskooi, D. Roundy, M. Ibanescu, P. Bermel, J. D. Joannopoulos, and S. G. Johnson, "Time-domain and frequency-domain modeling of nonlinear optical components on circuit-level using a node-based approach," Comp. Phys. Commun. **181**, 687–702 (2010).

1. Introduction

On-chip optical computation has the potential to outperform electronics in speed, bandwidth and power use. However, nonlinear photonic components still do not reach the high yield standards of their electronic counterpart, the transistor. One way of circumventing this problem, is shifting the computational paradigm. Instead of using a photonic version of the standard Von Neumann architecture, one can, for example, try to emulate neural networks on-chip [1]. The computational power of spiking neural networks (SNNs), a neural network type in which information is encoded in pulses, is comparable with a Turing machine [2]. A SNN consists of spiking neurons, i.e., excitable (nonlinear) dynamical systems [3]. As some photonic components are excitable [4, 5], they can be used to implement a spiking neuron in hardware.

In this paper, we focus on a simple Silicon-On-Insulator (SOI) microring. Due to heating and the thermo-optic effect, for sufficiently high input powers, bistable behaviour is obtained when the wavelength of the input signal is close to the resonance wavelength of the cavity. High Q-factor rings can even start to self-pulsate, as light will generate free carriers which will change the refractive index [6]. Similar to [4, 7], we will demonstrate how this self-pulsation is linked with excitability.

In literature the mechanism behind this self-pulsation (or excitability) in microrings, microdisks and similar passive cavities is often explained using Coupled Mode Theory (CMT). Time-domain simulations in this formalism show a good correspondence with experiments [8, 9, 10]. Moreover, the steady-state equations are still analytically solvable, both for varying power and wavelength of the input light. For SOI microdisks no hysteresis in the threshold of the input wavelength for the onset of oscillations is found, which indicates a supercritical Andronov-Hopf (AH) bifurcation [9]. In such a supercritical AH, a stable fixed point (FP) bifurcates to an unstable FP together with a stable limit cycle (LC), as opposed to a subcritical AH, where an unstable FP bifurcates into a stable FP together with a stable LC (with an unstable LC in-between) [3]. Both subtypes correspond to class II excitability in which the order of magnitude of the nearby self-pulsation period will be relatively unsensitive to the power or wavelength of the pump signal.

Moreover, the CMT-equations can be rewritten into the mean-field model used in [4, 7]. Using the steady-state curves and corresponding 2D projections of nullclines of this model, the class II excitability of a 2D Indium Phosphide (InP) Photonic Crystal (PhC) can be explained [7]. There as well, a sweep of the input wavelength indicates an AH bifurcation. Similar behaviour appears in PhC nanocavities [4].

As the computational properties of the microring in a spiking neuron usage are linked to the relevant bifurcation types [3], we will focus on the bifurcation type at the onset of self-pulsation,

for varying input power and fixed input wavelength. This takes into account that, on a photonic chip, information is encoded in the amplitude and phase of the light, while the wavelength rather corresponds with the choice of channel the information is transferred in. Classifying this bifurcation allows us to predict how the microring can be excited by input signals [3]. This helps to understand how it could process information in a (photonic) spiking neural network. Furthermore we focus on the cascadability of these optical spiking neuron units.

The rest of this paper is structured as follows. We first write down the CMT-equations for a microring, as this formalism allows to incorporate the contributions of all the relevant physical effects in a very intuitive way. We then show how the relevant nullclines for this system can be obtained using phase-plane analysis which is a useful tool to investigate the dynamics of neurons [3]. Using the resulting phase portraits, we demonstrate how we can simplify the CMT-equations, while still preserving the relevant physics of the problem. Moreover, we use the phase portraits to identify the exact bifurcation type at the oscillation onset. Subsequently, we analyse some time-traces to illustrate how the microring can be excited. We then demonstrate that this excitability is cascadable and conclude with some experimental results which confirm the predictions from the simulations. In the appendices we provide numerical and mathematical details about the simulations. All the time-traces in this paper are simulated with Caphe, a nonlinear component circuit simulator which we developed [11].

2. Microring: nonlinear behaviour

Optical bistability and self-pulsation in a SOI-microring has experimentally been demonstrated [6]. To explain this behaviour we use the CMT-description of a microring in which we include several physical effects. A first important effect in bulk silicon is two photon absorption (TPA), which generates free carriers. These free carriers are then able to absorb light by free carrier absorption (FCA). In addition, the presence of free carriers causes a blueshift in the wavelength by free carrier dispersion (FCD). In SOI microrings also (linear) surface state absorption at the silicon-silica interface is present, and at the same time some light is lost due to surface scattering and radiation loss [6]. The absorbed optical energy is mainly lost by thermalization, which generates heating. Due to the thermo-optic effect this heat results in a redshift in the resonance wavelength. The free carriers typically relax at least one order of magnitude faster than the temperature.

When the backscattering in the microring is neglected, the dynamics of the ring can be described in CMT with one complex variable (the mode amplitude $a = |a|e^{j\phi}$, with $|a|^2$ the energy in the cavity and ϕ the phase), and two real variables (the mode-averaged temperature difference with the surroundings ΔT and the amount of free carriers N). In this paper, we study an All-Pass (AP) filter with one input: a single ring coupled with only one bus waveguide. The CMT-equations are then [9, 10, 12]:

$$\frac{da}{dt} = \left[j(\omega_r + \delta\omega_{nl} - \omega) - \frac{\gamma_{loss}}{2} \right] a + \kappa s_{in}, \tag{1}$$

$$\frac{d\Delta T}{dt} = -\frac{\Delta T}{\tau_{th}} + \frac{\Gamma_{th}\gamma_{abs}|a|^2}{\rho_{Si}c_{p,Si}V_{th}}, \tag{2}$$

$$\frac{dN}{dt} = -\frac{N}{\tau_{fc}} + \frac{\Gamma_{FCA}\beta_{Si}c^2|a|^4}{2\hbar\omega V_{FCA}^2 n_g^2}, \tag{3}$$

$$s_{out} = e^{j\phi_c}s_{in} + \kappa a, \tag{4}$$

with s_{in} the amplitude of the input light (input power $P_{in} = |s_{in}|^2$), s_{out} the amplitude of the output light (output power $P_{out} = |s_{out}|^2$), ϕ_c the phase propagation in the bus waveguide, κ the

coupling from waveguide to ring, $\omega_r = \frac{2\pi c}{\lambda_r}$ the resonance frequency of the cavity and $\omega = \frac{2\pi c}{\lambda}$ the frequency of the input light. τ_{th} and τ_{fc} are the relaxation times for resp. the temperature and the free carriers. β_{Si} is the constant governing TPA, $c_{p,Si}$ the thermal capacity, ρ_{Si} the density of silicon and n_g is the group index. We neglect dispersion and take $n_g = n_{Si}$, with n_{Si} the refractive index of bulk silicon. We also use the effective volumes V_α and confinements Γ_α corresponding with a physical effect α defined in [9]. In Eqs. (1) and (2) γ_{loss} and γ_{abs} are resp. the total loss and absorption loss in the cavity, with:

$$\gamma_{loss} = \gamma_{coup} + \gamma_{rad} + \gamma_{abs}, \tag{5}$$

where we have introduced the coupling loss into the waveguide γ_{coup} (with $\kappa = j\sqrt{\gamma_{coup}e^{j\phi_c}}$) and the radiation loss γ_{rad}. In the ring we have absorption by linear surface absorption, TPA and FCA :

$$\gamma_{abs} = \gamma_{abs,lin} + \Gamma_{TPA}\frac{\beta_{Si}c^2|a|^2}{n_g^2 V_{TPA}} + \Gamma_{FCA}\frac{\sigma_{Si}c}{n_g}N, \tag{6}$$

σ_{Si} is the absorption cross section of FCA and $\gamma_{abs,lin}$ the linear absorption constant. In SOI $\eta_{lin} = \frac{\gamma_{abs,lin}}{\gamma_{abs,lin}+\gamma_{rad}} \approx 0.4$ [6, 12], so we use this value throughout the paper. The thermo-optic effect and FCD both cause a relevant shift in the resonance frequency ω_r, while the shift caused by the Kerr-effect is negligible. In first order perturbation theory, this gives:

$$\frac{\delta\omega_{nl}}{\omega_r} = -\frac{1}{n_g}\left(\frac{dn_{Si}}{dT}\Delta T + \frac{dn_{Si}}{dN}N\right). \tag{7}$$

Setting the derivatives to zero in Eqs. (1)-(3) results in the steady-state equations. These can be solved analytically. From Eq. (3) N is easy calculable if we know $|a|$, which can, together with $|a|$, be used to calculate ΔT. If we keep the input wavelength λ fixed and put $\frac{da}{dt} = 0$ in Eq. (1), we can rewrite the result as:

$$\left[j\left(\omega_r + \delta\omega_{nl}(\Delta T, N)\right) - \omega\right) - \frac{\gamma_{loss}(|a|,N)}{2}\right]a = -\kappa s_{in}. \tag{8}$$

If we now take the square of the modulus of both sides we get, independent of ϕ:

$$\left[(\omega_r + \delta\omega_{nl}(\Delta T, N) - \omega)^2 + \left(\frac{\gamma_{loss}(|a|,N)}{2}\right)^2\right]|a|^2 = |\kappa s_{in}|^2. \tag{9}$$

As $P_{in} = |s_{in}|^2$, the right hand side of Eq. (9) is linear in the input power. Given that Eq. (6) and 7 are linear in ΔT and N, the left hand side is a quadratic function of ΔT and N and a higher order polynomial in $|a|^2$. To obtain the steady-state curves we can thus simply parameterize ΔT, N and P_{in} as a function of $|a|^2$. When we substitute those values in Eq. (8), we can calculate ϕ. In high Q-rings ($Q > 2 - 3 \times 10^4$) TPA generates enough free carriers to make FCD prominent for sufficiently high input powers. We will illustrate the concepts of this paper with simulations for such a SOI $4\,\mu$m-radius microring with $540\,\text{nm} \times 220\,\text{nm}$ cross section waveguides. This ring has a resonance width $\lambda_{3dB} = 25\,\text{pm}$ at the resonance wavelength $\lambda_r = 1552.770\,\text{nm}$. We consider a critically coupled ring with $\gamma_{coup} = \gamma_{abs,lin} + \gamma_{rad}$. Details can be found in Appendix A.

Figure 1 shows the relation between input and output power, where we clearly see bistable behaviour. This bistability is mainly caused by the thermo-optic effect, while free carrier effects rather influence the appearance of self-pulsation. Indeed, as the light energy both heats up the cavity and generates free carriers, and the thermo-optic and FCD have an opposite influence
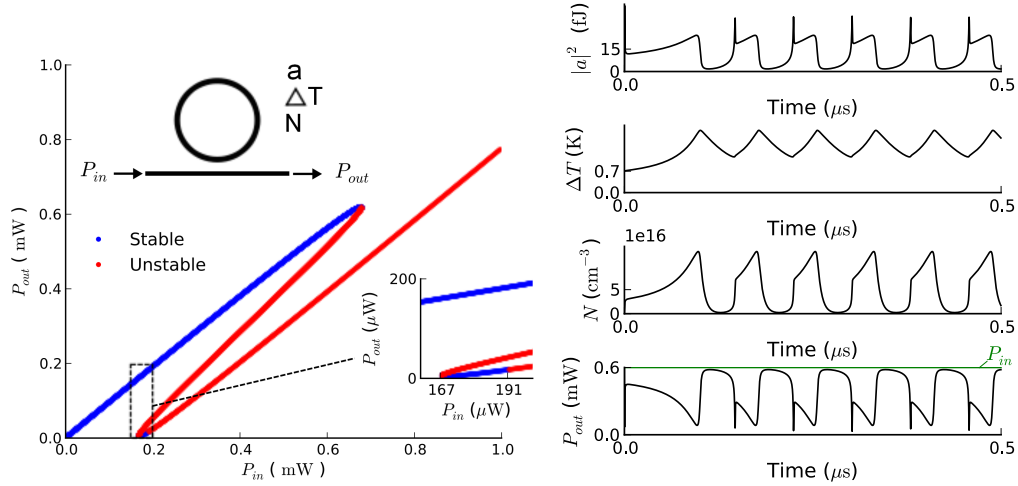
Fig. 1. For detuning $\lambda - \lambda_r = 62\,\text{pm}$, $P_{out}(P_{in})$ is bistable (left figure), for $P_{in} > 191\,\mu\text{W}$ the lower P_{out}-branch becomes unstable, which is an indication of self-pulsation. For $P_{in} = 0.6\,\text{mW}$ and $(a, \Delta T, N)(t{=}0){=}(0, 0.7, 0)$ this gives the self-pulsation time-traces on the right.

on the effective resonance wavelength (and thus the amount of light coupled into the cavity), self-pulsation is possible with a mostly asymmetric pulse shape, caused by the difference in timescale between the fast free carrier generation and absorption of optical power and the slow relaxation of the temperature in the cavity. For lower input powers, in the bistability region, there can be two stable FPs in combination with an unstable one ($P_{in} = 167 - 191\,\mu\text{W}$) or one stable FP together with two unstable FPs and a stable LC ($P_{in} > 191\,\mu\text{W}$, LC not included in the figure). For higher input powers there are no stable FPs and the ring will always self-pulsate.

3. Phase-plane analysis

Similar to [7], to gain more insight in the CMT-equations, we now construct 2D-phase portraits, which will be used in the subsequent paragraphs. Therefore, we project the $(a, \Delta T, N)$-time-traces for a given input power and wavelength onto the $(\Delta T, N)$-plane. Moreover, we calculate the $d(\Delta T, N)/dt = 0$, $d(\Delta T, a)/dt = 0$ and $d(N, a)/dt = 0$ nullclines (details in Appendix B). Where the three curves intersect we have steady-state FPs. $d(N, a)/dt = 0$ and $d(\Delta T, a)/dt = 0$ only intersect in the $(\Delta T, N)$-plane in those FPs (Fig. 2, proof given in Appendix C).

Moreover, both the temperature time constant ($\tau_{th} = 65\,\text{ns}$) and the free carrier relaxation time ($\tau_{fc} = 5.3\,\text{ns}$) are bigger than the time constants governing the dynamics of the light ($\eta_{lin}\tau_{abs,lin} = \tau_{coup} = 2/\gamma_{coup} = 205\,ps$, and the detuning of the light corresponds with a time constant of the same order of magnitude). After a very short transient period $\approx 100\,ps$ $da/dt \approx 0$, the $(a, \Delta T, N)(t)$ solutions are then converged to the $da/dt = 0$ surface. We can thus use the projections of the $d(\Delta N, a)/dt = 0$ and $d(\Delta T, a)/dt = 0$ nullclines to the $(\Delta T, N)$-plane to do standard 2D phase-plane analysis.

Time-traces follow both the $d(\Delta T, N)/dt$ directions on the $da/dt = 0$-surface and the corresponding direction changes indicated by the nullclines (Fig. 2). As N reacts faster than ΔT, the time-traces often relax towards the $d(N, a)/dt = 0$ nullcline. Consequently, during the self-pulsation the ring makes steep transitions in-between the upper and lower $d(N, a)/dt = 0$-branch.
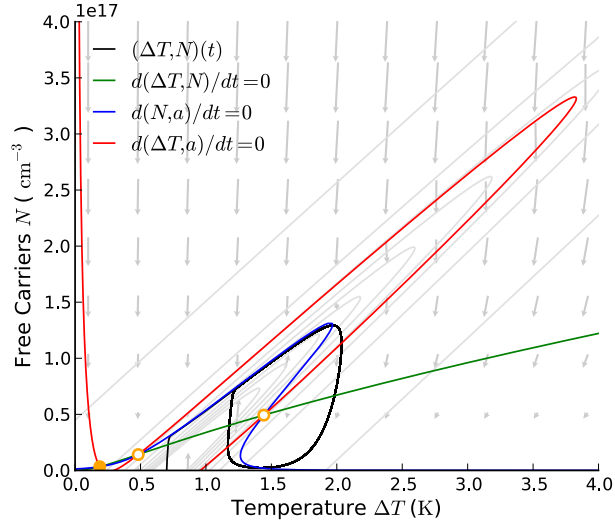
Fig. 2. On the phase portrait for $P_{in} = 0.6\,\text{mW}$ and a $62\,\text{pm}$ detuning, the $d(N,a)/dt = 0$, $d(\Delta T,a)/dt = 0$ nullclines only intersect at the three FPs (orange circles). In correspondence with Fig. 1 two of those FPs are unstable (open circle), while one is stable (filled circle). The example time-trace from Fig. 1 (black line) clearly follows both the $d(\Delta T,N)/dt$ directions on the $da/dt = 0$-surface (grey arrows) and the corresponding direction changes indicated by the nullclines. Moreover, (grey) contour lines of $da/dt = 0$ for $|a|^2 = 1\,\text{fJ} - 31\,\text{fJ}$ are elliptic and do not overlap (Appendix C).

4. 2D approximation

In section 3 we have explained why we can do phase-plane analysis in the $(\Delta T,N)$-space. The same arguments can now be used to do a dimensionality reduction, by doing an adiabatic elimination of the field variable a (a basic center manifold projection technique [13]). To simplify the equations we neglect the TPA-contribution in γ_{loss} in Eq. (6) (details included in Appendix D). In this system we still see self-pulsation (Fig. 3), so at longer timescales (above $100\,\text{ps}$) the most relevant physics is conserved.

This 2D system can be used to calculate the separatrix of the microring (discussed in section 3), by starting close to the unstable saddle and integrating backwards in time (Fig. 3).

This reduction in the number of variables not only simplifies the phase-plane analysis, but in addition allows a speed-up of simulations of huge circuits containing these microrings. By eliminating the fast timescale from the system, the integration step can increase without relevant accuracy loss. In addition, fewer variables need to be stored. Finally, this 2D-approximation is an extra justification for our 2D phase-plane analysis. Although qualitatively similar results are obtained with this 2D-approximation, the simulations in the body of this paper are still done with the full 4D-system.

5. Bifurcation analysis of the onset of bistability and the onset of self-pulsation

For a given input power the microring can have one, two or three FPs (Fig. 1 and Fig. 4). The microring undergoes a Saddle-Node bifurcation (SN) if it has two FPs. If it has three FPs, at least one (at low $|a|$) is stable. When two of the three FPs are unstable, there is a stable LC around the high $|a|$-FP. The middle FP will always be unstable, and is a saddle-node. It has an unstable manifold which ends at the low $|a|$ stable FP and, if there is one, at the upper LC, or
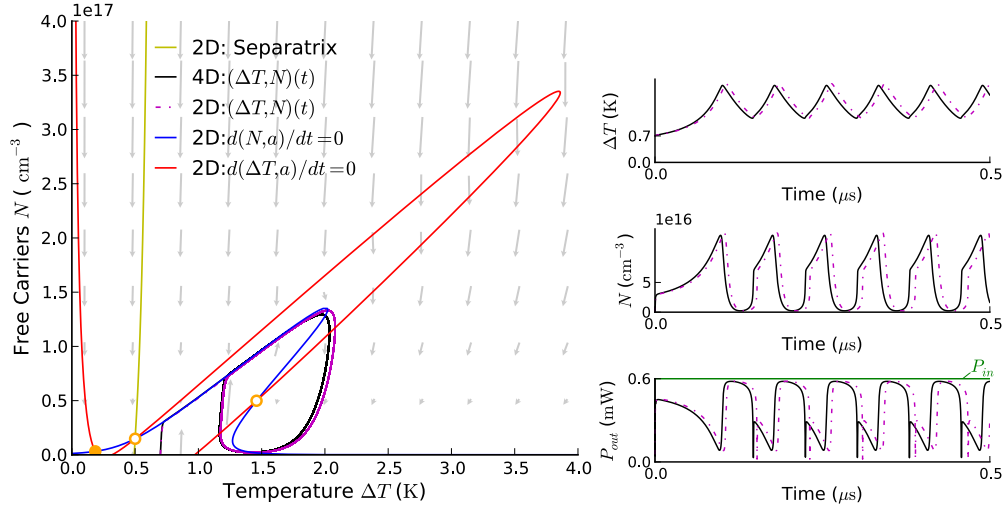
Fig. 3. The phase portrait obtained by neglecting the TPA-contribution in γ_{loss} in Eq. (6), looks similar to Fig. 2 and still explains (approximately) the dynamic behaviour of the time-trace of the 4D-system from Fig. 1 (black line). Furthermore, the time-trace with a corresponding initial condition in the 2D-approximation (dashed magenta lines) follows qualitative the 4D-behaviour, both in phase-plane and in time-domain, although the shape of the limit cycle (LC) is slightly different. The yellow line is the separatrix of the simplified system.
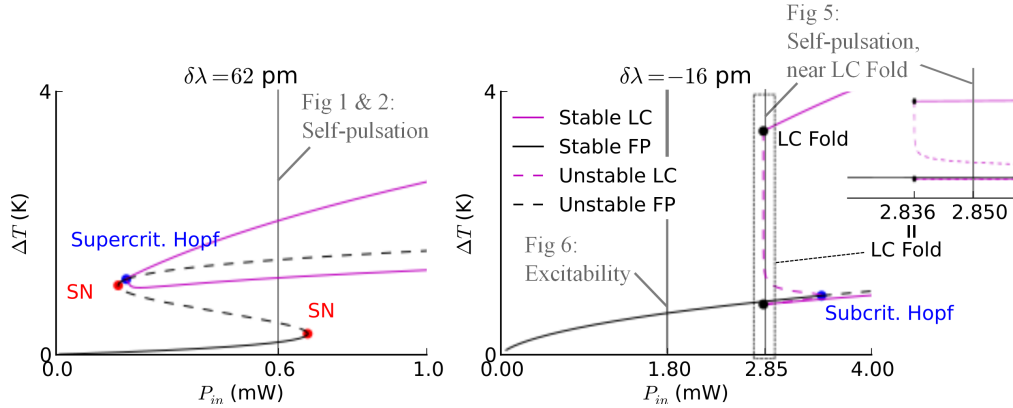

Fig. 4. At the red side of the resonance (e.g., left: $\delta\lambda = 62$ pm) the Andronov-Hopf (AH) bifurcation (blue dot) tends to be supercritical, while it can be subcritical at the blue side of the resonance (e.g., right: $\delta\lambda = -16$ pm). FPs (black) and the extreme values of the LCs (magenta) in a $\Delta T(P_{in})$-bifurcation diagram, calculated using PyDSTool [14], illustrate this. Moreover, at $\delta\lambda = 62$ pm the ring is bistable in-between two Saddle-Node (SN) bifurcations (red dots), while at $\delta\lambda = -16$ pm a stable and unstable LC annihilate in a LC Fold bifurcation at $P_{in} = 2.836$ mW (black dots). Relevant P_{in}-values used in the other figures are indicated.

else, at the high $|a|$ stable FP. A stable manifold or separatrix divides the basins of attraction of the lower FP and the higher $|a|$ FP/LC. If there is only one FP and it is unstable, then there is a stable LC around it.

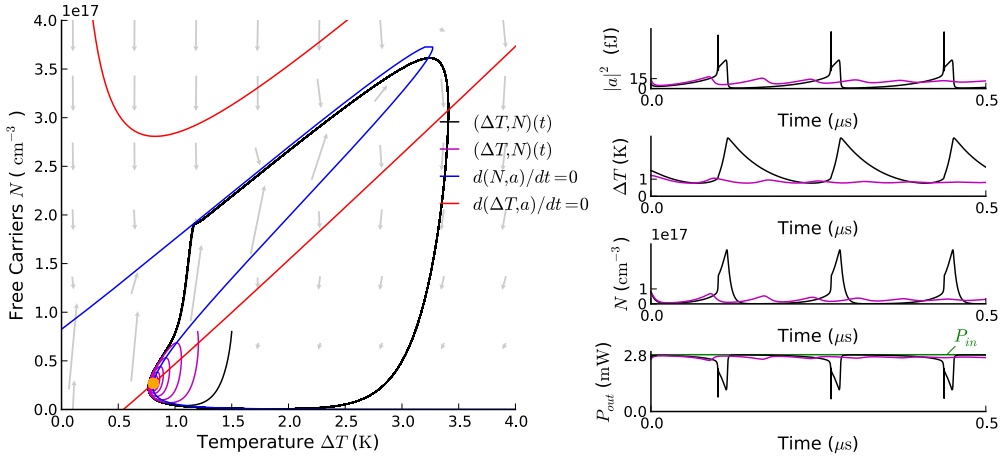For some wavelengths, the onset of oscillation shows hysteresis in the input power, which is

Fig. 5. For some input powers and wavelength settings the LC encloses a stable FP (filled circle) in the $(\Delta T, N)$ phase-plane. This indicates a subcritical AH bifurcation. We illustrate this here for $P_{in} = 2.85$ mW and $\delta\lambda = -16$ pm. Depending on the initial conditions, the trajectory will converge to the LC (black curve $(\Delta T, N)(t{=}0) = (1.5\,\text{K}, 8\text{e}16\,\text{cm}^{-3})$) or to the FP (magenta curve $(\Delta T, N)(t{=}0) = (1.2\,\text{K}, 8\text{e}16\,\text{cm}^{-3})$).

a sign of a subcritical AH bifurcation, in contrast to the regions without this hysteresis which correspond to a supercritical AH bifurcation. Given the previous ring parameters, if the input light is detuned towards the blue, where there is no bistability, typically a subcritical AH bifurcation appears. However, if the input light is detuned towards the red, in the bistability region, a supercritical AH bifurcation appears (this corresponds to the supercritical AH bifurcation reported in [9]). In the case of the subcritical AH bifurcation, a stable LC coexists with a stable FP centered in this LC. This can be proved explicitly with time-traces for, e.g., $P_{in} = 2.85$ mW at a $\delta\lambda = -16$ pm detuning, where we have one stable FP and a stable LC. By choosing the initial conditions within a subregion of the region defined by the LC on the $da/dt = 0$ surface we can end in the central FP or in the LC (Fig. 5). The basin of attraction of the stable FP is determined by an unstable LC (not included in figure) in-between the stable LC and this FP. The stable and unstable LCs annihilate in a fold LC bifurcation for lower input powers (e.g., at $P_{in} = 2.836$ mW for $\delta\lambda = -16$ pm in Fig. 4).

6. Excitability

In the wavelength region where the self-pulsation hysteresis is present, the microring is excitable if the input power is below, but close to, the fold LC bifurcation (Fig. 6, with a $T_{tr} = 2$ ns long power increase of P_{in} from 1.8 mW to 2.9 mW as perturbation, modelled by making s_{in} time dependent in Eq. (1)). For these input settings a small perturbation will kick the ring out of its rest state, into a 'ghost' of a LC pulse, whereafter the system will return to the initial rest state. In this power region there does not yet exist a stable LC, but the phase-plane already incorporates similar dynamics, as we are close to the bifurcation point. A look at the pulse-trajectory in the phase-plane clearly illustrates this similarity (Fig. 6). Being near to an AH bifurcation, similar to the excitability reported in [4], this is class II excitability [3].
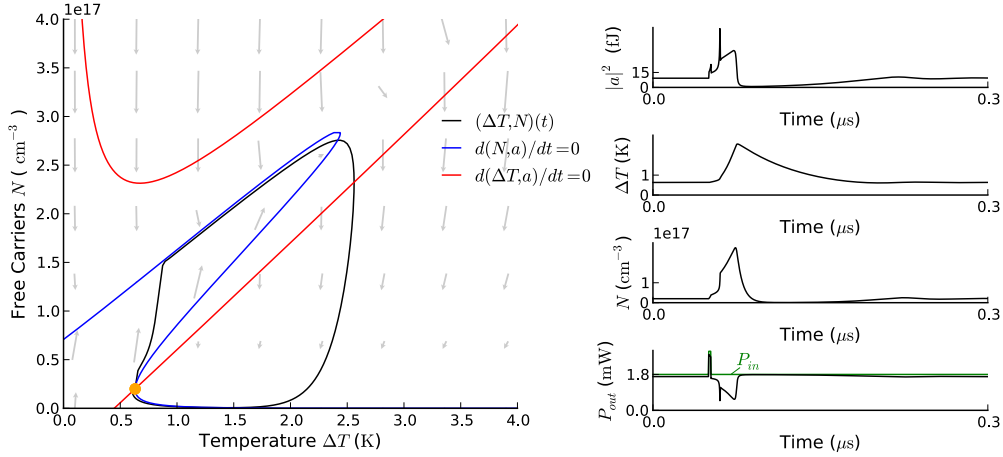
Fig. 6. A temporary increase from $P_{in} = 1.8\,\text{mW}$ to $2.9\,\text{mW}$ at $\delta\lambda = -16\,\text{pm}$, during $2\,\text{ns}$, triggers an excitation. Although for this input power no LC is present, the excitation can be seen as a reminiscent of the nearby LC from Fig. 5.
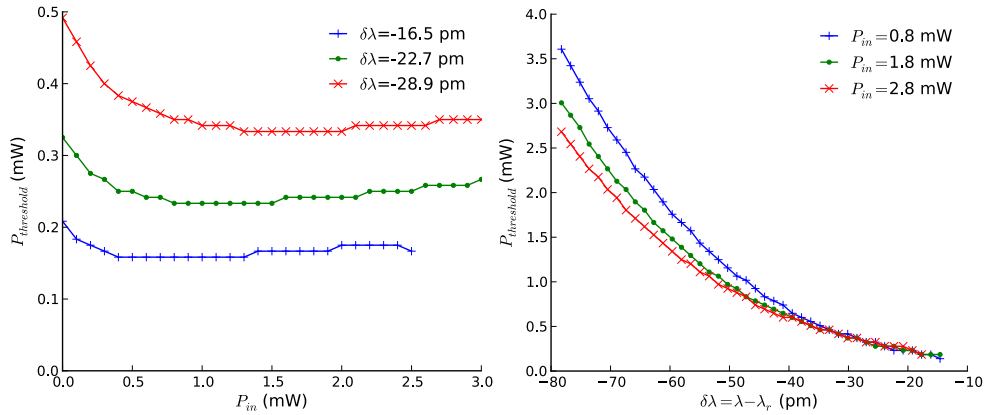

Fig. 7. The excitability-threshold power $P_{threshold}$ is more λ than P_{in} dependent. Trigger pulses are $T_{tr} = 10\,\text{ns}$ long and have been send in the opposite direction as the pump light.

6.1. Threshold

Characteristic for this kind of excitability is that the precise shape of the perturbation is rather unimportant. As long as the perturbation is strong enough, the shape of the ring's excitation is not influenced by the input-pulse shape. For a given $T_{tr} = 10\,\text{ns}$ we can determine the threshold $P_{threshold}$ in the trigger power P_{tr}. Below this threshold no excitation will be triggered (and the response on the perturbation will be trigger pulse dependent), above this threshold the ring is excited. We simulate this by sending pulses with varying P_{tr}-height, with the trigger wavelength $\lambda_{tr} = \lambda$, in the opposite direction of the pump light (this simplifies the comparison of $P_{threshold}$ for different P_{in}). This can be easily modelled by incorporating an extra version of Eq. (1) for the counterpropagating mode in the ring [10]. We neglect backscattering in the ring.

To approximate $P_{threshold}$, we calculate the peak temperature after a pulse, i.e. $h = max(\Delta T(t > t_{pulse}))$, and keep track for which P_{tr}-value dh/dP_{tr} is maximum. This approximation is based on the observation that perturbations above threshold induce a remarkable stronger temperature

increase than sub-threshold perturbations. In the low P_{in}-region there is no 'real' excitability, as the shape of the system's output pulse again becomes dependent on P_{tr}. However, as this transition between excitability and no excitability is rather smooth, the used threshold-approximation algorithm can still detect a 'threshold', which apparently slightly increases. For small detunings high P_{in} generate a stable LC, we therefore exclude those points from the graphs.

In principle, $P_{threshold}$ should increase if the distance with the LC fold bifurcation increases. This effect is rather negligible for a fixed λ if P_{in} decreases, but is present for a fixed P_{in} if λ decreases (Fig. 7). The more λ is detuned from λ_r, the higher the input power needed to reach this bifurcation point, and thus the higher the threshold.
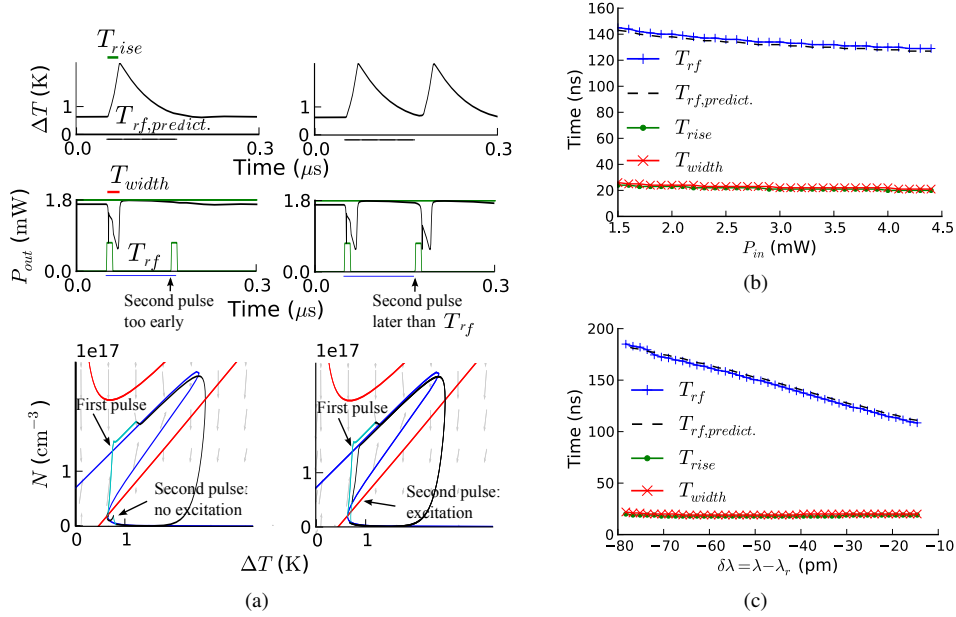
6.2. Refractory time

Fig. 8. The refractory time T_{rf} is the time after a pulse during which the ring is insensitive to a second perturbation (a). It is on the order of magnitude of τ_{th}, and is not much power dependent for $\delta\lambda = -35\,\text{pm}$ (b), while there is a clear wavelength dependency for $P_{in} = 1.8\,\text{mW}$ (c). The refractory time can be predicted by looking at the time needed for $\Delta T(t)$ to relax to the rest state ($T_{rf,predict.}$). Moreover, the width of the pulse T_{width} is proportional to the rise time of the temperature, i.e., the time needed to reach the maximum temperature after a pulse. In the phase portrait we indicate the trajectory the ring makes during the external perturbations with cyan, while we use black for the rest of the response.

If, after an excitation, the microring did not yet relax to the rest state, it is insensitive to new excitations (Fig. 8). The refractory time T_{rf} is the time during which an excitable system is insensitive to new pulses after an excitation. T_{rf} is rather insensitive to P_{in}, but increases with decreasing λ. As $\Delta T(t)$ is the slowest variable of the system, we can link the order of magnitude of T_{rf} to the thermal relaxation time τ_{th}: after an excitation, the ring is only sensitive to new perturbations if its temperature has sufficiently decreased, so it is close enough to its rest state. Consequently, T_{rf} can be predicted by the time needed for a ring to return to the initial rest state after a pulse ($T_{rf,predict.}$). Moreover, the pulse width T_{width} seems to be proportional to the rise time, i.e., the time the temperature needs after an excitation to reach the maximum value (Fig.

8). We do not see the proportionality of T_{rf} with T_{width}, measured in PhC nanocavities [4].
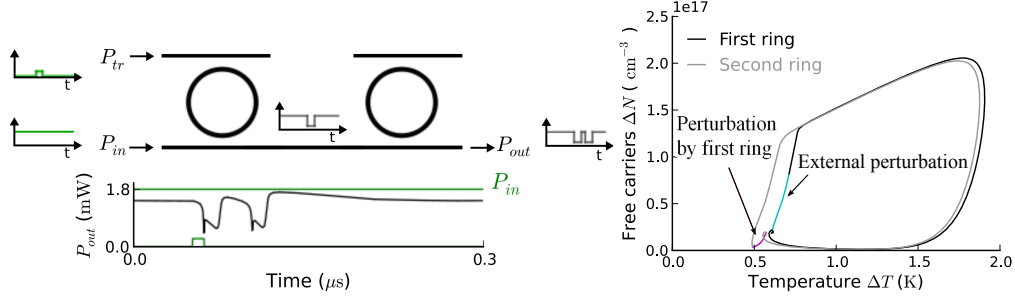
6.3. Cascadability

Fig. 9. If a ring is excited by a trigger signal, this excitation can excite another ring. To demonstrate this we send a CW pump signal with $P_{in} = 1.8\,\text{mW}$ and $\delta\lambda = -16\,\text{pm}$ through the common bus of a series of two AD filters. By exciting the first ring via the drop port (with a 10 ns trigger with $P_{tr} = 250\,\mu\text{W}$, $\lambda_{tr} = \lambda$) we guarantee that the external trigger pulse never reaches the second ring. The second pulse in the circuit's output, which corresponds to the second ring's excitation, is thus triggered by the first pulse, originating from the first ring. In contrast to the perturbation of the first ring (caused by the trigger), the second ring is initially perturbed (by the first ring) towards lower ΔT and N (right phase portrait). This causes the delay between the two excitations to be bigger than the delay between the trigger and the first pulse (time-trace bottom left).

Since the precise shape of the trigger pulse is less important, the output pulse of a ring can serve as a trigger pulse of another ring. If the trigger pulse is on the common bus waveguide, it is impossible to distinguish whether the last ring is excited by the input trigger or by the first ring's excitation. To circumvent this problem we use a circuit with two Add-Drop (AD) filters with common bus waveguide and excite the first ring in such a way that the input pulse never reaches the second ring. The two rings have identical settings, and the extra coupling section has the same τ_{coup} as in the previous simulations. In this setup the first ring clearly excites the second one, which makes this excitability mechanism cascadable (Fig. 9). Moreover, the second ring is perturbed in a different manner than the first one: the trajectory is initially kicked towards lower ΔT and N (phase portrait Fig. 9). This results in a longer time-lapse between this pulse and its perturbation (the first ring's excitation) than the time-lapse between the first ring's pulse and its perturbation (the external trigger). Other (not included) simulations indicate that for this pump signal the resonance wavelength of both rings can differ slightly ($\sim 0.2\delta\lambda_{3dB,AD}$).

7. Experimental verification of simulation results

7.1. Measurement setup

To test the previous single ring simulation results we designed an AP ring with a 550 nm × 220 nm cross section, a $4.5\,\mu\text{m}$ radius, a 250 nm gap, with a bus waveguide bended with the same curvature as the ring. This ring has a resonance at 1530.708 nm with $\delta\lambda_{3dB} \approx 20\,\text{pm}$ (with resonance splitting $\delta\lambda_{ps} \approx 20\,\text{pm}$) and an 8 dB extinction ratio. A temperature controller, which guarantees the chip temperature deviations to be below $\pm 0.03\,\text{K}$, is used to prevent drift of the resonance wavelength (Fig. 10). Light of a tunable laser (TL) is coupled in and out the chip via grating couplers. The ring output is measured with a 10 GHz photodiode and visualized with a 1 GHz real-time scope, as we expect a $\sim 10\,\text{MHz}$ signal. A similar setup is used in the double ring experiments.
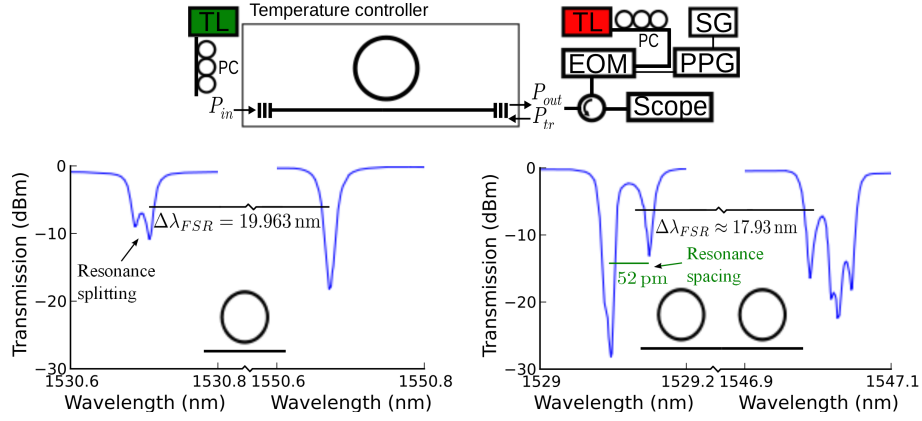
Fig. 10. Schematic of the setup for a single ring measurement. Light of a tunable laser (TL), polarized with polarization controllers (PC) is coupled in and out the chip via grating couplers (GC). The ring output is measured with a 10 GHz photodiode and visualized with a 1 GHz real-time scope. In the excitability experiment a second TL is used, mostly coupled in the opposite direction via a circulator. The pulses are created using a signal generator (SG) and a pulse pattern generator (PPG) and an electro-optical modulator (EOM). At the bottom, spectral details of both the single ring (left figure) and double ring resonances (right figure), used in this paper, are included.
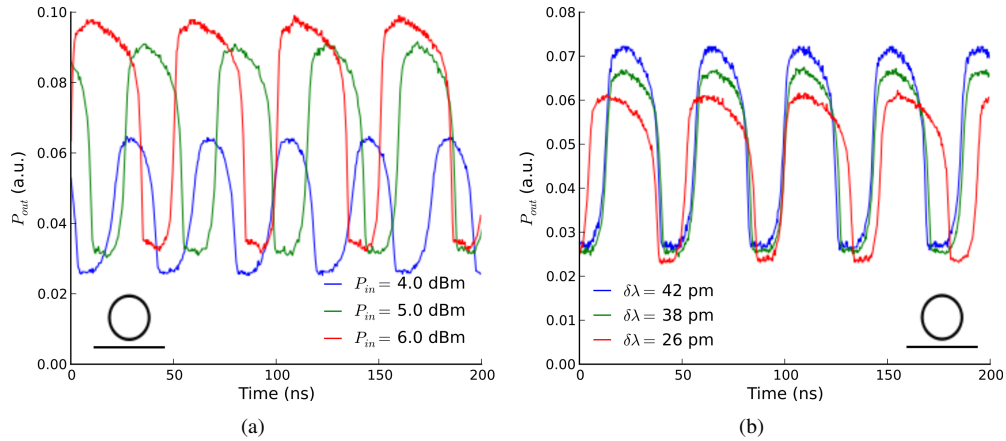
7.2. Single microring self-pulsation

Fig. 11. Both the input power and wavelength clearly change the pulse shape and period of the self-pulsation in an AP ring with a $550\,\text{nm} \times 220\,\text{nm}$ cross section, a $4.5\,\mu\text{m}$ radius, near the resonance wavelength at $1530.708\,\text{nm}$. (a) Input power sweep with pump wavelength detuning $\delta\lambda = \lambda - \lambda_r = 40\,\text{pm}$. Power values are those at the output of the laser. Due to the grating coupler the on-chip input power of the ring is expected to be $\sim 6\,\text{dB}$ lower. (b) Detuning sweep of the same ring with $5.0\,\text{dBm}$ output power at the TL laser. The self-pulsation period is in the order of $\sim 50\,\text{ns}$.

Both the input power and wavelength clearly change the pulse shape and period of the self-pulsation (Fig. 11). The self-pulsation period is in the order of $\sim 50\,\text{ns}$, which is a little bit

faster than the period in our simulations. We thus expect τ_{th} to be slightly smaller. The on-chip powers for these self-pulsation traces are in the order of $\sim 0.6 - 1\,\text{mW}$, as predicted by our simulations. These input powers are thus comparable with those needed for self-pulsation in PhC nanocavities, while this ring self-pulsates one order of magnitude faster [4].

The experimental pulse shape differs slightly from the simulated one due to a different ring geometry and pump setting, adapting the simulation parameters to the experimental chip design can eliminate this difference [9, 10]. Furthermore, the limited range of the self-pulsation period, which is finite at the self-pulsation onset confirms the presence of the AH-bifurcation.
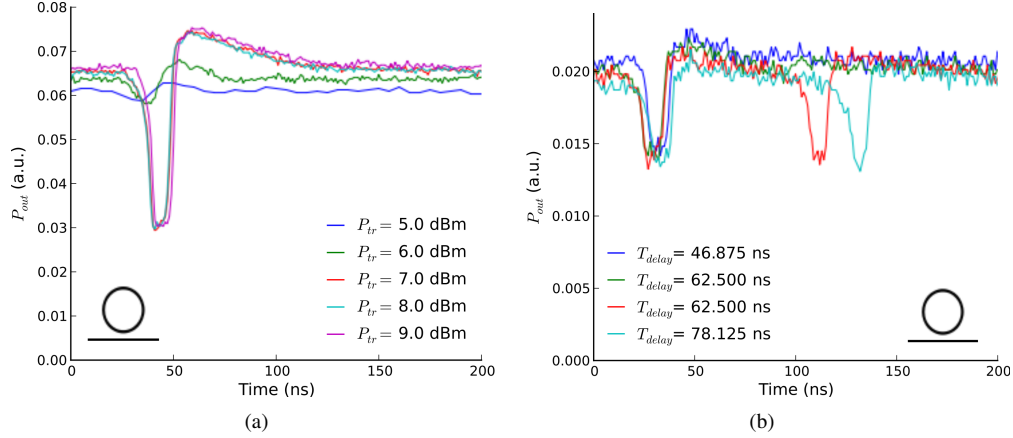
7.3. Single microring excitability

(a)   (b)

Fig. 12. (a) If the trigger power is sufficiently high ($\geq 7\,\text{dBm@TL}$) the ring excites with a fixed pulse shape, while for lower trigger powers subthreshold oscillations are visible. The 4 dBm pump light is detuned at $\delta\lambda = -4\,\text{pm}$ from the $\lambda_r = 1530.708\,\text{nm}$ resonance. The trigger light is tuned $\delta\lambda_{tr} = 9\,\text{pm}$ near another ring resonance at $\lambda_{r'} = 1550.671\,\text{nm}$. (b) The refractory time is on the order of magnitude of the self-pulsation period. The pump settings are similar to (a), while the trigger pulse settings are $\delta\lambda_{tr} = 9\,\text{pm}$ and $P_{tr} = 5\,\text{dBm}$. Mentioned power values are those at the output of the lasers, due to GCs and EOM the on-chip input power of the ring is expected to be $\sim 6\,\text{dB}$ lower for the pump light and $\sim 14\,\text{dB}$ lower for the trigger signal.

To verify the excitability of the rings we detune the pump wavelength with an input power near the self-pulsation onset. If we are too close to this onset, excitations triggered by noise can be perceived, but the purpose is to trigger the excitations by an external optical signal. For instance, sending rectangular trigger pulses with a 15.625 ns width and 250 ns period at a wavelength 'close' to one of the resonances of the ring can excite the ring (in this paper we trigger at another ring resonance, as this allows to filter out the trigger light, but triggering at the same resonance also works). To create these trigger pulses another TL is modulated with an electro-optical modulator (EOM), we therefore generate a 16-bit signal (a single 1 and 15 0's, unless otherwise mentioned) with a pulse pattern generator (PPG) of which the clock is fixed by a signal generator (SG) at 64 MHz. Although the pulse width of the trigger signal is rather big compared to the thermal timescale, experiments show that the pulse shape is independent of this width. The on-chip pulse-energy threshold for excitability is $\sim 3\,\text{pJ}$ (Fig. 12(a)).

If the delay between two trigger pulses (T_{delay}) is too small, the second pulse does not excite the ring (Fig. 12(b), the second pulse is created by putting an extra bit to 1 on the PPG). Therefore we can infer the refractory time to be somewhere around 60 ns, i.e. on the order of magnitude

of the self-pulsation period. This all confirms the initial assumption in our simulations that τ_{th} is $\sim 60\,\text{ns}$. It is difficult to measure this refractory time more accurately with this setup, as noise makes the ring response ambiguous: e.g., at a $62.5\,\text{ns}$ delay the second pulse can sometimes excite the ring, but sometimes fails to do this.

In 12(b) an extra optical tunable filter with passband at $1530\,\text{nm}$ is placed before the photodiode, comparison to 12(a) confirms that reflection of the trigger pulses in the circulator to the photodiode can be neglected.
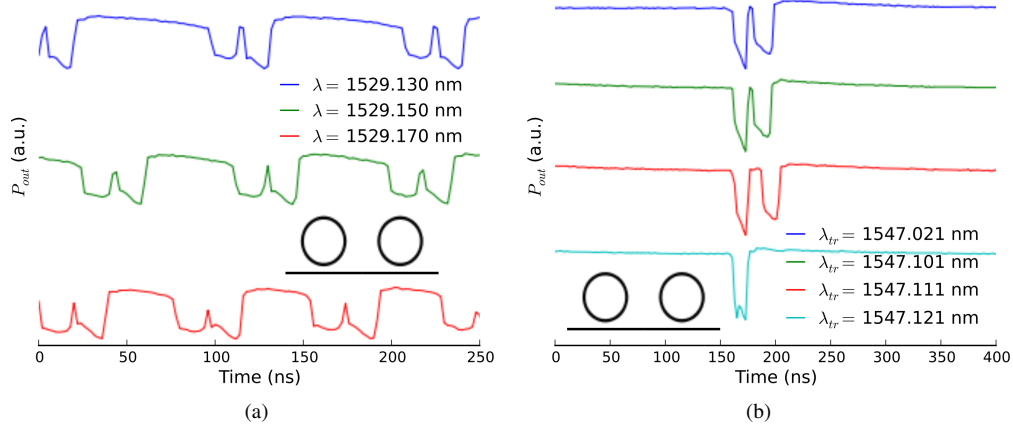
7.4. Cascadable microring excitability

Fig. 13. If the resonances of two identical AP rings with common bus waveguide are close enough to each other they will show self-pulsation (a) and excitability (b) for the same pump wavelength and power. Both rings have a $5.0\,\mu\text{m}$ radius. The self-pulsation is measured at $10.5\,\text{dBm@TL}$ (this starts at $\sim 1529.120\,\text{nm}$ and ends around $1529.260\,\text{nm}$ in hysteresis with single ring self-pulsation), the excitability with the pump at $\lambda = 1529.007\,\text{nm}$ and $P_{in} = 13.60\,\text{dBm}$, while $P_{tr} = 12.00\,\text{dBm}$. Trigger pulse and pump light are now co-directional. On-chip powers are therefore expected to be resp. $10.00\,\text{dB}$ and $18.00\,\text{dB}$ lower, as $\sim 4\,\text{dB}$ is lost in a splitter used to combine pump and trigger signals.

To experimentally investigate the cascadability of ring excitability, we did similar measurements of two identical AP rings with a $550\,\text{nm} \times 220\,\text{nm}$ cross section, a $5.0\,\mu\text{m}$ radius, and a $225\,\text{nm}$ gap, connected to the same bus waveguide. The spacing of the ring resonances at $\sim 1529\,\text{nm}$ is $52\,\text{pm}$, while $\lambda_{3dB} \approx 30\,\text{pm}$ (Fig 10). Similar rings on this chip sometimes had a $> 1\,\text{nm}$ spacing, as this value is determined by the process variation statistics. For some pump settings the rings self-pulsate in a synchronized way, with one fixed period ($\lambda = 1529.130 - 1529.170\,\text{nm}$ in Fig 13(a)). Moreover, for some pump settings they are both excitable for the same input power and wavelength (e.g., over a $\sim 90\,\text{pm}$ λ_{tr}-region in the upper three curves in Fig 13(b)). Indeed, given the small (compared to the refractory time) and rather fixed time-lapse between the two pulses, comparison to the single ring excitability experiments suggests that the second pulse is not triggered by noise and the two pulses thus have to originate from different rings. This illustrates the experimental feasability of the simulation result from Fig. 9, where an AD ring circuit is used.

However, in contrast to the AD-configuration from Fig. 9, in the currently measured AP-configuration it is impossible to unambiguously trigger the first ring without directly perturbing the second one, even if we change the wavelength of the trigger pulse. Indeed, both rings have

nominally the same radius and thus the same free spectral range. Therefore, if the excitability regions and regions where the ring is sensitive to trigger pulses overlap at one resonance, they also overlap at all the other resonances. Subsequently, it is nontrivial to identify to which rings the resonances belong and trigger them individually. A difference in ring radius or the usage of AD rings can circumvent this problem.

The second ring thus feels both the external trigger pulse and the excitation of the first ring. From Fig. 9 we know that the external trigger will result in an initial ΔT and N increase, while the first ring's excitation kicks the second ring's trajectory initially towards lower ΔT and N, which results in a longer time-lapse between the two excitations. The $\sim 15 - 20$ ns delay between the excitations in the upper three curves from Fig. 13(b) indicates that the excitation of the first ring is strong enough to perturb the trajectory of the second ring sufficiently to induce this longer time-lapse, clearly showing the cascadable transfer of information from the excitation of the first ring to the second ring. Indeed, the $47.1\,\mu$m center-to-center distance of the rings results in a 0.7 ps latency between the two rings, so if the last ring was only perturbed by the trigger pulse the two excitations should almost coincide.

Furthermore, we can simulate a similar trigger situation by cascading two AP rings and trigger them with a small P_{in} perturbation through the common bus (Fig. 14). The trigger pulse excites both rings, but the excitation of the first ring kicks the trajectory of the second ring back to lower N. Consequently, the excitation of the second ring is delayed and therefore does not coincide with the first ring's excitation.

If the trigger wavelength is in a < 10 pm region around 1547.121 nm (bottom curve Fig. 13(b)),
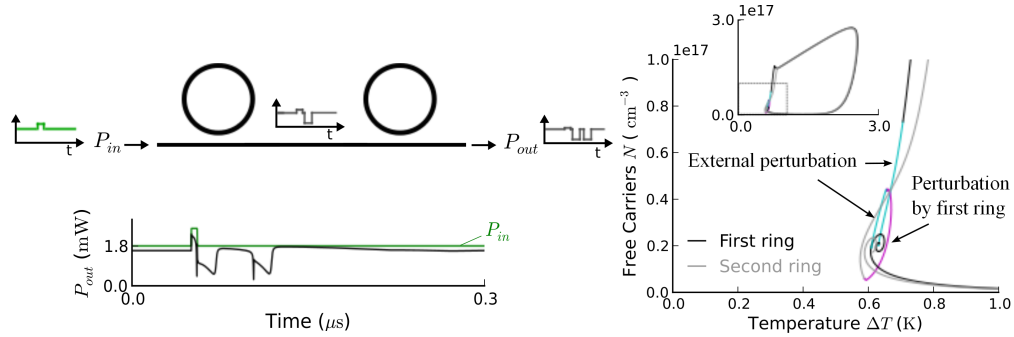

Fig. 14. Triggering two cascaded AP rings through the common bus with a 5 ns power increase from 1.8 mW to 2.59 mW at $\delta\lambda = -16$ pm results in a similar time-lapse between two pulses in the time-trace (left) as in Fig 9. The phase-plane (right) clearly illustrates how the excitation of the first ring delays the excitation of the second ring, by kicking its trajectory towards lower N.

only one pulse is visible. This pulse can correspond to a single ring excitation (the trigger excites only one ring), or with a coincident double ring excitation (the trigger excites both rings directly and the first ring had no influence on the second one). Further research is needed to explain this time-trace more thoroughly, but in all likelihood the trigger signal is detuned too far from resonance for the excitability to be cascadable.

Measurements of similar ring pairs with a > 100 pm resonance spacing reveal regions with synchronized self-pulsation, but no regions with coexisting excitability. Measurements of ring pairs with a > 1 nm resonance spacing even fail to show synchronized self-pulsation.

8. Conclusions

A high Q microring self-pulsates for certain input power and wavelength settings, which can be described with CMT, using three variables: the complex mode amplitude a of the light in the cavity, the temperature difference with the surrounding ΔT and the amount of free carriers N. Neglecting the fast energy and phase dynamics of the light allows a 2D phase-plane analysis. Furthermore, this dimensionality reduction provides a manner to construct two new equations of motion for ΔT and N, which still capture the most important dynamics.

For some wavelengths, when changing the input power, the microring undergoes a subcritical Andronov-Hopf bifurcation at the self-pulsation onset. As a consequence the system shows class II excitability. This thorough understanding of the excitability mechanism will allow a correct characterization of the computational properties of a microring, used as a photonic spiking neuron.

Simulations show that this excitation mechanism is cascadable. Experimental single ring excitability and self-pulsation behaviour follows the theoretic predictions. Moreover, two identical rings can be excitable or self-pulsate for the same pump power and wavelength, if only their resonance spacing is sufficiently small ($< 100\,\text{pm}$). Ring pair circuits are proposed in which the trigger pulse can address only one ring directly, without perturbing the other one.

Appendices

A. Numerical details of the simulations

The ring geometry in our simulations is inspired by the one measured in [6]. The effective volumes and confinements are calculated using Meep FDTD [15], while the other material parameter values are based on [6, 9, 12]. This results in the parameter values in Table 1. For the AP filter we assume critical coupling, while the AD filter has two coupling sections which both have the same τ_{coup} as coupling section in the AP filter.

B. Calculation of the nullclines

For $d(\Delta T, N)/dt = 0$ we can use the same parameterization of ΔT and N as a function of $|a|$ as for the steady-state case. When calculating $d(N, a)/dt = 0$ we use Eq. (3) to parameterize N as a function of $|a|$, substitute this in Eq. (9) and solve the quadratic equation for ΔT. $d(\Delta T, a)/dt = 0$ can be obtained by solving Eq. (2) to ΔT (which is then dependent both on $|a|$ and N), substituting this in Eq. (3) and solving the corresponding quadratic equation for N (which gives us $N(|a|)$) and resubstituting this in the expression for ΔT (finally only dependent on $|a|$). In all three cases it is thus possible to find a suitable parameterization of both ΔT and N as a function of $|a|$.

C. Proof of the bijection between (ΔT,N)-plane and $da/dt = 0$-surface

That $d(N, a)/dt = 0$ and $d(\Delta T, a)/dt = 0$ only intersect in the (ΔT,N)-plane in the FPs can be intuitively understood by considering the projection of the $da/dt = 0$ surface on the (ΔT,N)-plane. Eq. (9) is quadratic both in ΔT and N, and defines an ellipse for each $|a|$-value. As the coefficients for ΔT^2, N^2 and $\Delta T N$ are all proportional to $|a|^2$, the orientation of the principal axes is independent of $|a|$. However, the center of this ellipse and the global scaling factor of the axes both are monotonically $|a|$-dependent, so the size of the ellipse, e.g., shrinks for higher $|a|^2$. Apparently, in Fig. 2, this dependence is in such a way that ellipses corresponding with different $|a|$-values do not overlap. This has as a consequence that the projection of the $da/dt = 0$ surface on the (ΔT,N)-plane is a bijection. Both $d(\Delta T, a)/dt = 0$ and $d(N, a)/dt = 0$ lie on the $da/dt = 0$ surface and only intersect in the FPs. The intersections of their projections

Table 1. Values of the parameters used in the simulations.

Parameter	Value	Magnitude
β_{Si}	8.4×10^{-12}	$m \cdot W^{-1}$
$\frac{dn_{Si}}{dT}$	1.86×10^{-4}	K^{-1}
$\frac{dn_{Si}}{dN}$	-1.73×10^{-27}	m^3
σ_{Si}	10^{-21}	m^2
ρ_{Si}	2.33	$g \cdot cm^{-3}$
$c_{p,Si}$	0.7	$J \cdot g^{-1} \cdot K^{-1}$
$n_g = n_{Si}$	3.476	
η_{lin}	0.4	
λ_r	1552.770	nm
AP ring: λ_{3dB}	25	pm
AD ring: λ_{3dB}	37.5	pm
$\tau_{abs,lin} = \frac{2}{\gamma_{abs,lin}}$	$\frac{205}{\eta_{lin}}$	ps
$\tau_{coup} = \frac{2}{\gamma_{coup}}$	205	ps
τ_{th}	65	ns
τ_{fc}	5.3	ns
Γ_{th}	0.9355	
Γ_{TPA}	0.9964	
Γ_{FCA}	0.9996	
V_{th}	3.19	μm^3
V_{TPA}	2.59	μm^3
V_{FCA}	2.36	μm^3

thus uniquely correspond to those FPs. From Eq. (9) it can be proved that this bijection is valid for general P_{in} and ω settings. Indeed, for a given $(\Delta T, N)$ pair, Eq. (9) is a third order equation in $|a|^2$. Applying, e.g., Descartes' rule of signs, on the coefficients of this third order $|a|^2$-polynomial one can determine that, independent of P_{in} and ω, there always exist just one single real positive root, which implies that the projection of $da/dt = 0$ on the $(\Delta T, N)$-plane is indeed a bijection. Consequently, we can, for general P_{in} and ω settings, identify the FPs only by looking at the intersections of $d(N,a)/dt = 0$ and $d(\Delta T, a)/dt = 0$ in the $(\Delta T, N)$-plane.

D. Calculation details of the 2D approximation

Most of the time $da/dt \approx 0$, and $|a|$ is completely determined by the instantaneous value of ΔT and N. From Appendix C we know that, for a given $(\Delta T, N)$ pair, Eq. (9) has only one positive real root, such that this third order equation can be solved unambiguously to $|a|$. However, in this paper we simply neglect the TPA-contribution in γ_{loss} in Eq. (6), as its effect on the broadening of the resonance width is $1-2$ orders of magnitude smaller than the other relevant physical effects. This makes Eq. (9) linear in $|a|^2$. If we substitute $|a|$ in Eq. (2) and (3) with this approximative $|\hat{a}|(\Delta T, N)$, we get a 2D dynamical system as a function of ΔT and N.

Acknowledgments